Increased Mass Transport at Lithographically Defined 3-D Porous Carbon Electrodes

Xiaoyin Xiao,[†] Mark E. Roberts,[‡] David R. Wheeler,[†] Cody M. Washburn,[†] Thayne L. Edwards,[†] Susan M. Brozik,[†] Gabriel A. Montano,[||] Bruce C. Bunker,[§] D. Bruce Burckel,*[,†] and Ronen Polsky*[,†]

Department of Biosensors & Nanomaterials, Sandia National Laboratories, P.O. Box 5800, MS-0892 Albuquerque, New Mexico 87185, United States, Chemical and Biomolecular Engineering, Clemson University, Clemson, South Carolina 29634, United States, Center for Integrated Nanotechnology (CINT), Sandia National Laboratories, 1515 Eubank Blvd SE, Albuquerque, New Mexico 87185, United States and Center for Integrated Nanotechnologies, Los Alamos National Laboratory, K771 Los Alamos, New Mexico 87545, United States

ABSTRACT Increased mass transport due to hemispherical diffusion is observed to occur in 3D porous carbon electrodes defined by interferometric lithography. Enhanced catalytic methanol oxidation, after modifying the porous carbon with palladium nanoparticles, and uncharacteristically uniform conducting polymer deposition into the structures are demonstrated. Both examples result in two regions of hierarchical porosity that can be created to maximize surface area, via nanostructuring, within the extended porous network, while taking advantage of hemispherical diffusion through the open pores.

KEYWORDS: carbon • porous electrodes • interference lithography • methanol oxidation • conducting polymers

INTRODUCTION

There are many reasons to fabricate nano-tailored microstructures. For instance, the nano- and/or microstructuring of electrodes can lead to high surface area and catalytically active interfaces. This structuring has been achieved in many ways: tuning catalytic particle size and shape (1, 2), fabricating catalytic surfaces in porous networks (3−7), or dispersing catalytic particles into porous templates (8, 9). However, due to small pore diameters, pore nonuniformity, and possible hydrophobicity, diffusion or penetration of the electrolyte is rarely uniform in many synthetic (nano)mesoporous materials, thereby limiting any advantage in increasing the surface area or modifying the structures with functional materials such as catalytic particles or large biomolecules. Another reason to fabricate nano- and/or micro- features is to influence the diffusion-driven mass transport of reactants such as fuels or analytes. Structures containing at least one dimension smaller than the Nernst diffusion layer thickness can experience hemispherical diffusion profiles that result in increased mass transport (10). While decreasing pore sizes and employing ensembles of smaller structures can provide increased active surface areas, they are often fabricated with a high density that produces overlapping diffusion layers, resulting in decreased mass transport (linear diffusion) profiles (11, 12). Thus, an inherent trade-off exists between maximizing surface area and preserving favorable hemispherical diffusion characteristics (13). We report here the fabrication and characterization of 3D carbon electrodes with interconnected porosity that combines the advantages of nanostructuring with increased mass transport. The unique highly ordered nanostructures provide increased pathways for reaction species to diffuse and react throughout entire catalyst-modified electrode surfaces and exhibit microelectrode response characteristics, which we demonstrate to be effective for increased catalytic oxidation of methanol and uncharacteristically uniform deposition of the conducting polymer.

We previously published detailed fabrication techniques for 3D carbon substrates, fabricated by means of interferometric lithography (14). Briefly, commercial photoresist was spin-coated on plasma cleaned silicon wafers and exposed to an interference pattern generated by interfering beams from a Q-switched Nd:YAG laser. This process was repeated iteratively prior to development to generate a multilayer structure. The photoresist was then pyrolyzed at 1100 °C for 1 h in forming gas (5% H_2 and 95% N_2). The resulting conducting carbon electrode consists of five interconnected layers of ~800 nm hexagonal pores. The connecting arms are ~80 nm in diameter in the top layer and ~300 nm in the bottom layer; the separation distance between individual layers (arms) is approximately 60 nm (detailed images of the top and cross-section of the electrodes are shown in the Supporting Information, Figure s1). Other methods exist for creating porous carbon structures with similar size scales to those of the patterns presented here, such as templating carbonaceous resins or recorcinol formaldehyde solutions into colloidal silica or polystyrene crystals (15, 16). While

* To whom correspondence should be addressed. E-mail: rpolsky@sandia.gov (R.P.); dbburck@sandia.gov (D.B.B.).
Received for review July 27, 2010 and accepted September 24, 2010
[†] Department of Biosensors & Nanomaterials, Sandia National Laboratories.
[‡] Department of Chemical and Biomolecular Engineering,Clemson University.
[§] Center for Integrated Nanotechnology (CINT), Sandia National Laboratories.
[||] Los Alamos National Laboratory.
DOI: 10.1021/am1006595

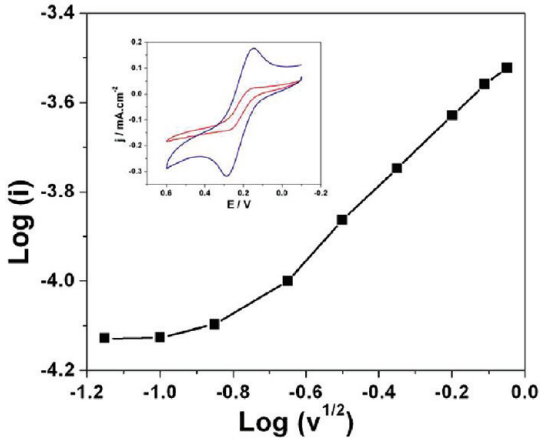

FIGURE 1. Plot of log current (*i*) versus log square root of scan rate ($\nu^{1/2}$). Inset: Cyclic voltammograms of 3D porous carbon in 1 mM ferrocene +0.1 M TBATFB. Scan rate: 5 and 50 mV/s (red and blue line, respectively).

the hexagonal porous 3-D carbon electrodes presented here are similar to templated structures, preparing the substrates lithographically does have some advantages. First, the interferometric lithography approach naturally creates large area, defect-free patterns, where template approaches suffer from a lack of long-range order. More importantly, the pore-to-arm ratio of the lithographically prepared substrates can be controlled through exposure dose and development conditions at a fixed lattice spacing, which affords the ability to tune the relative size of the pore-to-arm dimension. Finally, the carbon pores presented here are somewhat larger than those that have been reported from colloidal template approaches and provide an excellent platform to study the diffusional mass-transport profiles inside the structures, as discussed in the following sections. Pyrolyzed photoresist films are also known to have potential surface chemistry benefits such as atomically flat surfaces with a high degree of hydrogen termination, which we have previously demonstrated leads to smaller and more uniform depositions of gold nanoparticles in both planar (17) and IL-fabricated porous films (14).

RESULTS AND DISCUSSION

Information about diffusional mass transport in the 3D porous carbon structures was examined from the voltammetric response in 1 mM ferrocene, which is presented in Figure 1. A plot of anodic peak current versus the square root of the scan rate (log i_p versus log $\nu^{1/2}$) shows a flat plateau region from 5 to 20 mV/s followed by a linear region up to 800 mV/s (18). At the flat plateau, the current is independent of scan rate and is indicative of hemispherical diffusion (19). This is also shown by the s-shaped voltammogram run at 5 mV/s (Figure 1 inset, red curve), which is a characteristic of increased mass transport. Other causes of increased mass transport which produce s-shaped voltammograms, such as stirring the solution or using a rotating disk electrode, are not applicable in these experiments, and therefore the voltammogram shape is attributed to hemispherical diffu-

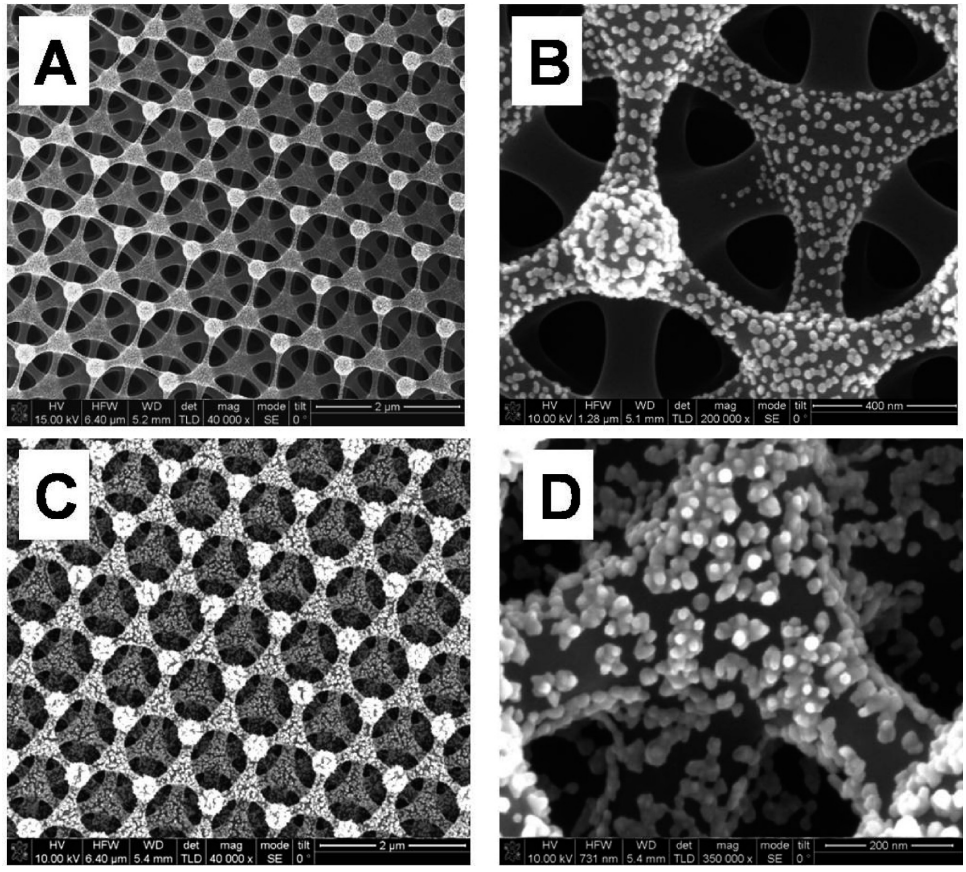

FIGURE 2. SEM images of Pd deposition onto 3-D porous carbon electrodes at a potential of −0.45 V for 100 s. (A,B) Deposition from 2 mM Pd/0.5 M H2SO4. (C,D) Deposition from 2 mM Pd/(MeCN + H_2O + 0.1 M HCl). Deposition potential, −0.45 V; deposition time, 100 s.

sion similar to what is observed at microelectrodes. The linear portion of the curve from 50 mV/s to 800 mV/s is representative of linear diffusion and typically produces peak-shaped voltammograms as shown by the scan at 50 mV/s (Figure 1 inset, blue curve). Remarkably, the electrode has a profile similar to a microelectrode despite the measured planar area in solution being ~0.5 cm^2. The gradual transition from hemispherical to lateral diffusion (or s-shaped to peak shaped voltammograms) upon the increase of scan rate is also typically observed in microelectrodes due to limiting conditions that are dependent on the time scale of the experiment (20, 21). Apparently, the pore sizes in our 3D nanostructures are sufficiently large enough to prevent an overlapping of the diffusion layers and preserve hemispherical diffusion at the nanometer scale arms and spokes. To our knowledge, similar diffusion-based studies have not been reported using structures prepared from templated polystyrene/silica sphere-based approaches. Hemispherical diffusion profiles are useful in acquiring high mass transport delivery of analytes, which we demonstrate with enhanced catalytic methanol oxidation at the 3D porous carbon electrodes after palladium nanoparticle modification.

Catalytic Pd particles were deposited onto porous 3D carbon electrodes from both aqueous and organic solvent solutions. Deposition at −0.45 V for 100 s was carried out in a 2 mM Pd/0.5 M H_2SO_4 aqueous solution (versus Ag/AgCl reference and Pt counter electrodes), which resulted in Pd deposition only on the top layers of the structures, as shown in Figure 2A,B. It is presumed that this inhomogeneous deposition is due to the hydrophobic carbon surface, which prevents the solution from penetrating into the inner pores, consistent with our previous observation where gold nanoparticles were deposited onto similar structures (17). Figure 2B shows that Pd particles are densely packed on the top two layers with decreased particle deposition on the third layer and no particles deposited on the connecting arms to the fourth layer. On the top two layers, most of the Pd particles are 2D clusters, an indication of 2D lateral growth. This is an indication of strong interaction of Pd nuclei with the carbon surface that likely prevents particle-like 3D growth. The particles on the third layer were sparse and unaggregated. The particle sizes and densities were largest on the top layer and decreased from the second to third layer, with the size of individual single Pd particles ranging from about 3 to 10 nm in diameter.

In order to achieve a more complete and uniform surface coverage of Pd particles throughout the entire porous carbon structure, a mixed solvent of acetonitrile (MeCN) and water was explored. MeCN was used to increase surface wettability, while a small amount of water was necessary to dissolve $PdCl_2$. A uniform deposition of Pd nanoparticles throughout the entire porous carbon structures was achieved in a MeCN/water mixture (90:10 vol %; versus Ag/$AgNO_3$ reference and Pt counter-electrodes), as shown in Figure 2C,D. The particle density and morphology is comparable to that shown in Figure 2B, indicating that the surface properties of the pyrolyzed carbon, and not the solution composition, dominate in Pd nucleation and subsequent 2D growth.

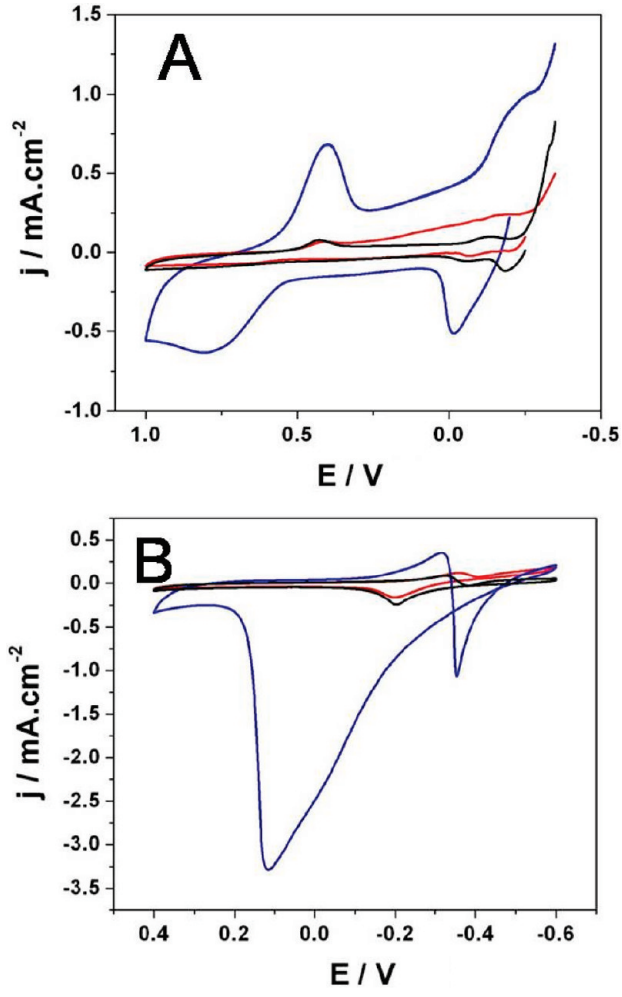

FIGURE 3. Cyclic voltammograms of Pd/3D (blue), Pd/2D (red), and Pd/GC (black) in 0.5 M $HClO_4$ (A) and 0.5 M NaOH + 0.3 M CH_3OH (B) at a scan rate of 50 mV/s.

We designate the above two as prepared Pd-modified electrodes shown in Figure 2A and C as Pd/2D and Pd/3D, respectively, for ease of description in subsequent discussion. Figure 3 shows the response from cycling in $HClO_4$ and the catalytic oxidation of methanol on Pd/3D, Pd/2D, and a glassy carbon electrode (Pd/GC), which was modified with Pd nanoparticles in an identical manner for a control substrate (blue, red, and black curves, respectively). The chemical structure and behavior of pyrolyzed photoresist films resembles that of glassy carbon, consisting of mostly amorphous carbon with small graphitic sp^2 and diamond-like sp^3 regions (22, 23), and has similar electrochemical properties (24). The Pd/2D electrode shows the same amplitude of current as the Pd/GC electrode in both systems, indicating that in this case there is not much advantage to the inhomogeneously coated porous carbon structure, as it behaves much like a planar electrode, which can be attributed to limited solution accessibility. The Pd/3D electrode, however, shows significant enhancement in catalytic current and in the charge that was transferred from methanol oxidation while exhibiting a positive peak shift which can be attributed to depressed diffusion kinetics. The accessible Pd catalytic

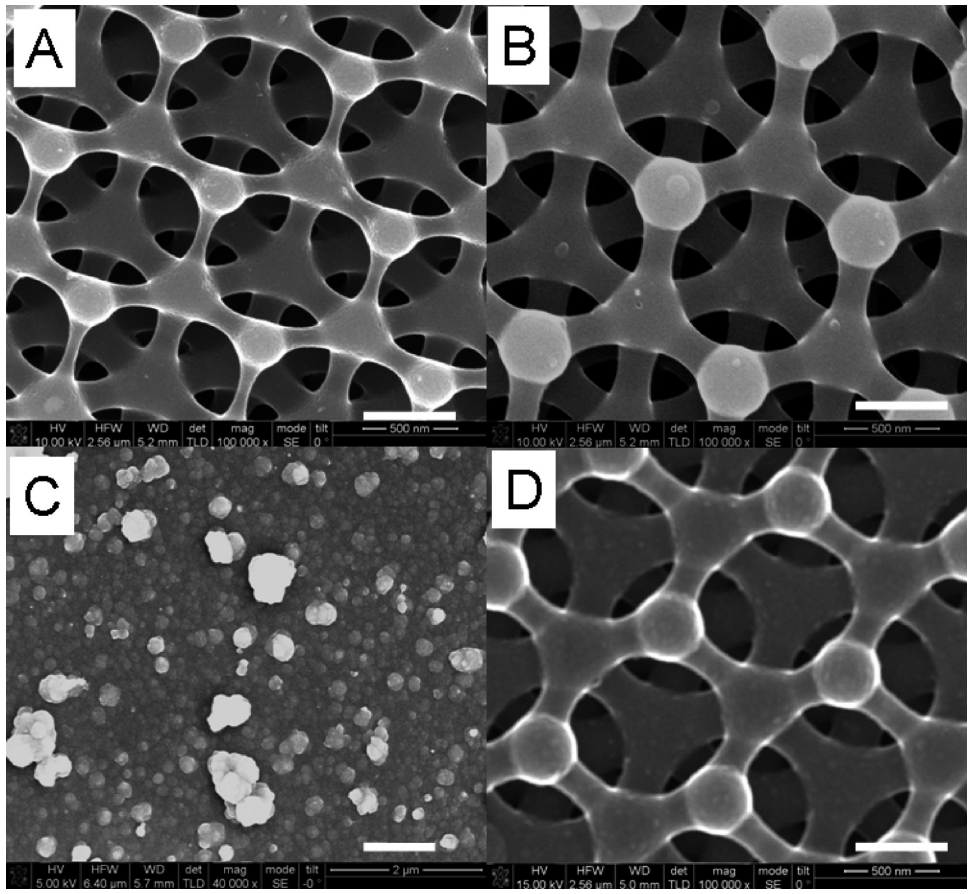

FIGURE 4. (A and B) Scanning electron micrographs of poly(bithiophene) deposition at 850 mV for 30 s (A) and 60 s (B). (C) Bithiophene deposition onto planar PPF at 850 mV for 60 s. (D) Poly(pyrrole) deposited using 2 cyclic voltammograms. Scale bars for A, B, and D = 500 nm and C = 1 μm.

surface area at the Pd/3D electrode is about 20 times that of the other two electrodes, as evaluated from the surface oxide desorption wave at ~0.4 V (cf. Figure 3A), 0.7×10^{-5} and 1.74×10^{-4} C cm^{-2}, respectively, while the amount of methanol being oxidized increases by a factor of 200 (cf. Figure 3B), 2.2×10^{-5} and 4.6×10^{-3} C cm^{-2}, respectively. If linear diffusion dominated, then the current due to methanol oxidation should be proportional to the increase of the surface area. Therefore, since the methanol oxidation at Pd/3D is 10 times greater than the increase in surface area over the 2D electrodes, the enhancement must be attributed to increased mass transport due to hemispherical diffusion within the nanostructured surfaces.

Another advantage of hemispherical diffusion is demonstrated using the 3D porous carbon structures as a scaffold for the electrochemical deposition of conducting polymers. It is well-known that mass transport plays a crucial role in the morphology of electrochemically deposited conducting polymer films whose growth resembles that of metals. Small islands or clusters initially nucleate on the electrode surface and then grow according to a 2-D or 3-D mechanism. The initial grains (or nuclei) eventually overlap, and the contiguous film growth proceeds in a 2-D manner for reaction-limited deposition conditions and a 3-D manner for diffusion limited conditions (25). Conducting polymers often exhibit 2-D growth on microelectrodes due to hemispherical diffusion of polymer precursors (26) and 3D growth as large asymmetric aggregates onto bulk electrodes. Fixed potential depositions of 10 mM bithiophene in 0.1 M $LiClO_4$/acetonitrile performed at 0.85 V (versus $Ag/AgNO_3$ reference and Pt counter electrodes) onto the 3-D porous carbon electrodes show unusually smooth and homogeneous films after 30 and 60 s of deposition when compared to the same depositions onto identical but planar pyrolyzed photoresist films, as shown in Figure 4A, B, and C, respectively. The polymer film thickness can be controlled with increasing deposition time. For instance, the SEM images indicate that the connecting arms on the top layer increase from ~74 nm in diameter to ~186 nm after 30 and 60 s of deposition (Figure 4A and B, respectively). We believe that the steady state mass transport of monomer molecules during deposition leads to the observed uniform 2-D film growth. Poly(pyrrole) also exhibits smooth films when deposited onto the porous carbon, similar to poly(bithiophene) shown in Figure 4D. It is worth noting that other groups have observed large asymmetric particle-like structures following poly(pyrrole) deposition onto microstructured pyrolyzed photoresist films (27), indicating that the unique structure of the 3D porous carbon electrodes is responsible for the homogeneous deposition, rather than the material properties of the films. High resolution SEM imaging confirms that the film deposits uniformly throughout the 3-D electrodes while retaining the open porous film structure, resulting in an overlaying nanoporous surface morphology on bare pyrolyzed carbon, presented

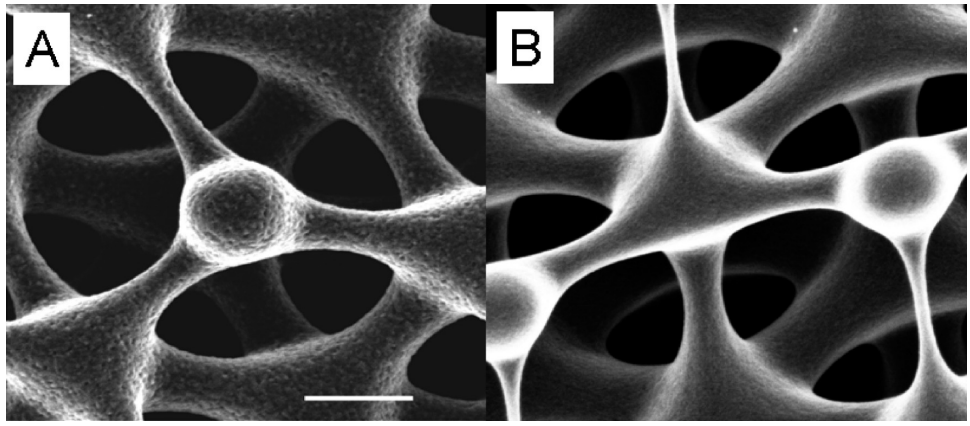

FIGURE 5. High magnification scanning electron micrographs after 30 s of bithiophene deposition on porous carbon at 850 mV (A) and bare porous carbon (B). Scale bar = 250 nm.

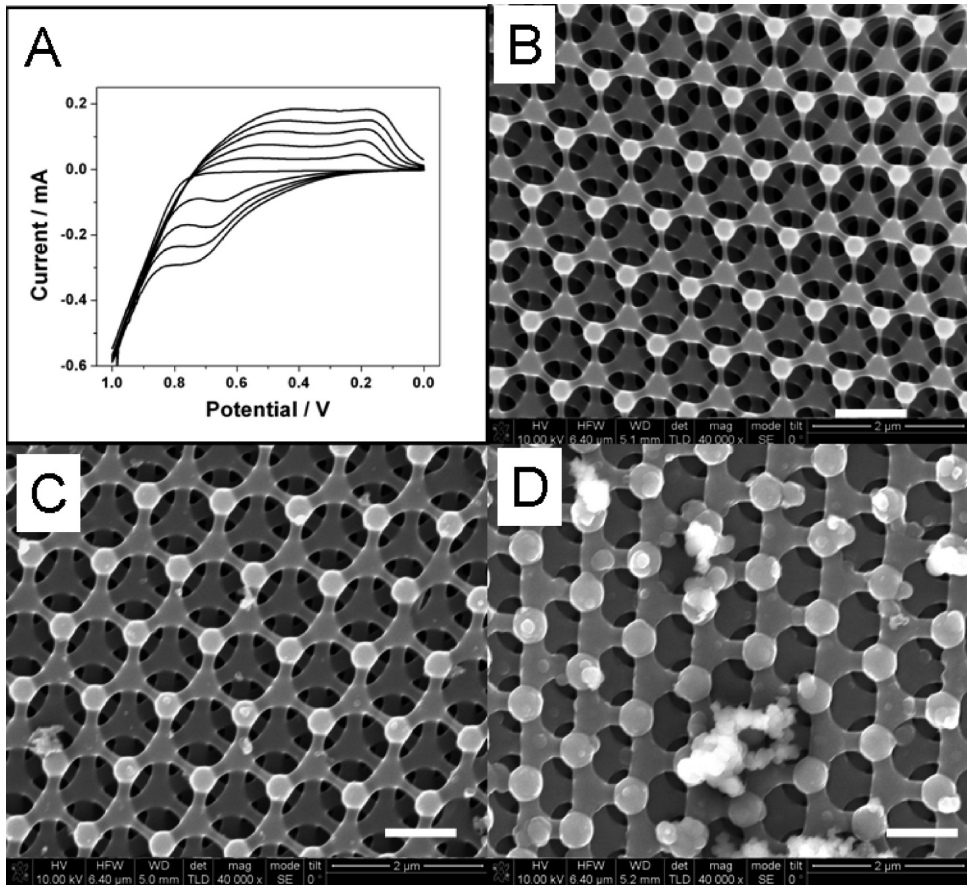

FIGURE 6. (A) Cyclic voltammograms of poly(bithiophene) deposition at a scan rate = 10 mV/s. Scanning electron micrographs of poly(bithiophene) deposition after 0, 2, and 5 cycles (B–D). Scale bar = 1 μm.

in Figure 5A and B, respectively. Therefore, two regions of hierarchical porosity can be created to maximize surface area, via nanostructuring onto the extended porous network, and still take advantage of hemispherical diffusion through the open pores. The film growth and thickness can also be precisely controlled by cyclic voltammametric deposition. As shown in Figure 6, the increasing current after each successive cycle indicates electrochemical film growth of bithiophene films, while the SEM images of the films electrochemically grown after 0, 2, and 5 potential cycles (from 0 to +1 V) show that the film thickness can be increased in a fashion that provides a means to control pore size. The film thickness remains relatively homogeneous at thinner films; however, occasional asymmetric 3D polymer growth increases with increasing film thickness. As the film thickness increases, eventually a point is reached where overlapping diffusion layers are created and 3D growth becomes favored, which further supports the purported mechanism that 2D growth is a result of hemispherical diffusion at the porous carbon electrodes.

In conclusion, we have shown here that the geometry of 3D carbon substrates, defined by interferometric lithography, can behave as microelectrodes, exhibiting hemispherical diffusion profiles that can lead to increased mass trans-

port capabilities while maintaining high surface area. Since such 3D porous carbon can be patterned at variable geometries (i.e., number of layers, separation distances between layers, arm diameter, layer thickness, etc.), these electrodes could have many advantages over synthetic (nano)mesoporous materials: (1) optimized pore sizes can be used to promote mass transport into inner pores; (2) they provide 3D high surface-area-to-loading capabilities for catalytic nanoparticles, leading to the full usage of the catalytic Pd particles over the entire porous structure; and (3) improved morphological film depositions for conducting polymers are achieved. We are investigating the opportunities these electrodes could offer in such areas as batteries, supercapacitors, biological sensors, and hydrogen storage devices.

METHODS

Materials and Instruments. All solutions were prepared with 18 MΩ water using a Barnstead Nanopure water purifier (Boston, MA). Isopropanol, acetonitrile, methanol, $PdCl_2$, tetrabutylammoniumtetrafluoroborate (TBATFB), HCl, pyrrole, $HClO_4$, and H_2SO_4 were purchased from Sigma. Bithiophene was purchased from Kodak. All electrochemical measurements were performed on a CH Instruments 660 Electrochemical Analyzer (Austin, TX) and were measured versus a Ag/AgCl in 3 M NaCl reference and a Pt counter-electrode from Bioanalytical Systems (West Lafayette, IN). Scanning electron microscope (SEM) imaging was performed on a Zeiss Supra 55VP field emission gun scanning electron microscope or an FEI Magellan 400 SEM.

Interferometric Lithography of 3D Porous Carbon Electrodes. A bottom antireflection coating (BARC), iCON-7 (Brewer Science, Rolla Missouri), was spun onto silicon wafers at 3000 rpm and baked on a vacuum hot plate at 205 °C for 60 s. Negative tone NR7 from Futurrex Inc. was used in all of the experiments. A thin layer of NR 7 100P (∼100 nm) was deposited and spun at 3000 rpm to create an adhesion layer. After flood exposure and a post exposure bake at 130 °C on a vacuum hot plate, a thick layer (6 μm) of NR7−6000P was deposited and spun at 3000 rpm and soft-baked at 130 °C. The frequency-tripled 355 nm line of a Q-switched Nd:YAG laser was used to form the interference pattern. The beam was expanded and split into two separate beams and interfered with an angle of 32° between the planewave propagation vectors. The plane of incidence contains both propagation vectors and the angle bisector of the propagation vectors, which is tilted with respect to the sample surface normal by 45°. After each exposure, the sample is rotated in the plane by 120°, and the process is repeated a total of three times. After exposure, the sample received a postexposure bake of 85 °C for 2 min on the vacuum hot plate. A 120 s puddle development, using RD-6 (Futurrex, Inc.) and spin drying, completed fabrication of the resist structures. The samples were baked on a hot plate at 180 °C for 30 min. The samples were then pyrolyzed at 1100 °C for 1 h in forming gas (5% H_2 and 95% N_2). Substrates were rinsed with isopropoanol and water before use.

Palladium Deposition. Pd was electrochemically deposited onto 3D porous carbon electrodes in both acidic water and a mixture of acetonitrile/water solutions. The electrode potential was fixed precisely at the point of the start of hydrogen evolution at carbon. The deposition was monitored by the increasing current due to Pd-induced hydrogen evolution.

Acknowledgment. Sandia is multiprogram laboratory operated by Sandia Corporation, a Lockheed Martin Company, for the United Stated Department of Energy's National Nuclear Security Administration under Contract DE-AC04-94AL85000. The authors acknowledge the Sandia National Laboratories' Laboratory Directed Research & Development (LDRD).

Note Added after ASAP Publication. This paper was published on the Web on October 14, 2010, with the wrong affiliation for Ronen Polsky. The corrected version was reposted on October 19, 2010.

Supporting Information Available: SEM images of the lithographically defined 3D carbon electrodes and a plot of current versus square root of scan rate of 1 mM Ferrocene + 0.1 M TBATFB versus $Ag/AgNO_3$ and platinum reference and counter-electrodes. This material is available free of charge via the Internet at http://pubs.acs.org.

REFERENCES AND NOTES

(1) Tian, N.; Zhou, Z. Y.; Sun, S. G.; Ding, Y.; Wang, Z. L. *Science* **2007**, *316*, 732.
(2) Goodman, D. W. *Nature* **2008**, *454*, 948.
(3) Adams, B.; Wu, G.; Nigrio, S.; Chen, A. *J. Am. Chem. Soc.* **2009**, *131*, 6930.
(4) Kiani, A.; Fard, E. N. *Electrochim. Acta* **2009**, *54*, 7254.
(5) Hakamada, M.; Mabuchi, M. *J. Alloys Compd.* **2009**, *479*, 326.
(6) Krishnamoorthy, K.; Zoski, C. G. *Anal. Chem.* **2005**, *77*, 5068.
(7) Park, S.; Song, Y. J.; Han, J. H. *Electrochim. Acta* **2010**, *55*, 2029.
(8) Niesz, K.; Koebel, M.; Somorjai, G. A. *Inorg. Chim. Acta* **2006**, *359*, 2683.
(9) Chu, S. Z.; Kawamura, H.; Mori, M. *J. Electrochem. Soc.* **2008**, *155*, D414.
(10) Wang, J. *Analytical Electrochemistry*, 3rd ed.; Wiley-VCH: New York, 2006.
(11) Menon, V.; Martin, C. R. *Anal. Chem.* **1995**, *67*, 1920.
(12) De Leo, M.; Kuhn, A.; Ugo, P. *Electroanalysis* **2007**, *19*, 227.
(13) Walcarius, A. *Anal. Bioanal. Chem.* **2010**, *396*, 261.
(14) Polsky, R.; Washburn, C. M.; Montano, G.; Liu, H. Q.; Edwards, T. L.; Lopez, D. M.; Harper, J. C.; Brozik, S. M.; Wheeler, D. R. *Small* **2009**, *5*, 2510.
(15) Chai, G. S.; Yoon, S. B.; Yu, J. S.; Choi, J. H.; Sung, Y. E. **2004**, *108*, 7074.
(16) Bauman, T. F.; Satcher, J. H. *J. Non-Cryst. Solids* **2004**, *350*, 120.
(17) Burckel, D. B.; Washburn, C. M.; Raub, A. K.; Brueck, S. R. J.; Wheeler, D. R.; Brozik, S. M.; Polsky, R. *Small* **2009**, *5*, 2792.
(18) Graph of (i vs $\nu^{1/2}$) can be found in the Supporting Information.
(19) (a) Zoski, C. *Handbook of Electrochemistry*; Elsevier: Amsterdam, 2006. (b) Davies, T. J.; Jones, S. W.; Banks, C. E.; Campo, J. D.; Mas, R.; Munoz, F. X.; Compton, R. G. *J. Electroanal. Chem.* **2005**, *585*, 51.
(20) (a) Penner, R. M.; Martin, C. R. *Anal. Chem.* **1987**, *59*, 2625. (b) Amatore, C.; Pebay, C.; Thouin, L.; Wang, A.; Warkocz, J. S. *Anal. Chem.* **2010**, *82*, 6933.
(21) (a) Ca, D. P.; Sun, L.; Cox, J. A. *Electrochim. Acta* **2006**, *51*, 2188. (b) Amatore, C.; Pebay, C.; Thouin, L.; Wang, A. *Electrochem. Commun.* **2009**, *11*, 1269.
(22) McCreery, R. L. *Chem. Rev.* **2008**, *108*, 2646.
(23) Ranganathan, S.; McCreery, R. L. *Anal. Chem.* **2001**, *73*, 893.
(24) Gui, A. L.; Liu, G. Z.; Chockalingam, M.; Saux, Le.; Harper, J. B.; Gooding, J. J. *Electroanalysis* **2010**, *22*, 1283.
(25) Harrison, J. A.; Thirsk, H. R. *Electroanalytical Chemistry*; Bard, A. J., Ed.; Marcel Dekker: New York, 1971; Vol. 5, p 67.
(26) Hwang, B. J.; Santhanam, R.; Lin, Y. L. *Electrochim. Acta* **2001**, *46*, 2843.
(27) Kinoshita, K.; Song, X.; Kim, J.; Inaba, M. *J. Power Sources* **1999**, *81−82*, 170.

AM1006595